

Mirror symmetric on-chip frequency circulation of light

Jason F. Herrmann^{1,*}, Vahid Ansari¹, Jiahui Wang¹, Jeremy D. Witmer¹, Shanhui Fan², and Amir H. Safavi-Naeini¹

1. Ginzton Laboratory and Department of Applied Physics, Stanford University, Stanford, CA 94305 USA

2. Ginzton Laboratory and Department of Electrical Engineering, Stanford University, Stanford, CA 94305 USA

(Dated: September 29, 2021)

Integrated circulators and isolators are important for developing on-chip optical technologies, such as laser cavities, communication systems, and quantum information processors. These devices appear to inherently require mirror symmetry breaking to separate backwards from forwards propagation, so existing implementations rely upon magnetic materials, or interactions driven by propagating waves. In contrast to previous work, we demonstrate a mirror symmetric nonreciprocal device. Our device comprises three coupled photonic resonators implemented in thin-film lithium niobate. Applying radio frequency modulation, we drive conversion between the frequency eigenmodes of this system. We measure nearly 40 dB of isolation for approximately 75 mW of RF power near 1550 nm. We simultaneously generate nonreciprocal conversion between all of the eigenmodes in order to demonstrate circulation. Mirror symmetric circulation significantly simplifies the fabrication and operation of nonreciprocal integrated devices. Finally, we consider applications of such on-chip isolators and circulators, such as full-duplex isolation within a single waveguide.

Circulators are nonreciprocal devices that allow propagating signals to cycle between three channels, *e.g.*, $\text{in}_1 \rightarrow \text{out}_3$, $\text{in}_3 \rightarrow \text{out}_2$, $\text{in}_2 \rightarrow \text{out}_1$ as shown in Fig. 1a. A circulator can isolate components from each other, *i.e.*, it can prevent reflections from returning to the source of a signal, simply by terminating one of its three channels through absorption. For example if we terminate port 2 in Fig. 1a, signals will propagate from $\text{in}_1 \rightarrow \text{out}_3$, but $\text{in}_3 \rightarrow \text{out}_2$ would be terminated, thereby preventing reflections on the third port from propagating back to the first port. There is flexibility in selecting the input and output channels. In many realizations, the channels in_k/out_k are the incoming and outgoing waves in the waveguides connected to port k . However, other realizations are also possible. In this work, our input channels correspond to the incoming waves at different frequencies in one waveguide (on the left in Fig. 1b), and the output channels correspond to the outgoing waves at different frequencies in the other side of the waveguide (on the right in Fig. 1b). Unlike more typical three-waveguide configurations, this type of circulator is compatible with *mirror symmetry*:¹ by imposing the same scattering relations between the frequency channels for light traveling from right to left in the device, we obtain a second frequency circulation, related to the first by reflection about the center axis (dashed line in Fig. 1b).

The mirror symmetry of our circulator means that its physical implementation can be simpler than more traditional circulators and isolators, which *require* mirror symmetry breaking. Many of these demonstrations use magnetic materials,^{2–7} traveling waves,^{8–18} or multiple modulators emitting with different phases^{19–23} to induce a sense of direction and nonreciprocal propagation. As a consequence of mirror symmetry in our device, a single radio frequency (RF) electro-optic modulator (EOM) is sufficient to generate circulation between three optical frequency channels. As we show here, this significantly simplifies hardware implementations of nonreciprocal photonic circuits.

Results

We demonstrate a device on a thin film lithium niobate (TFLN) platform that consists of three coupled photonic racetrack resonators. The first resonator is coupled to a bus waveguide, as shown in Fig. 1c. The modes of racetrack resonators 1 (2) and 2 (3) are coupled at a rate μ_{12} (μ_{23}), while 1 and 3 are not directly coupled ($\mu_{13} = 0$). Our device uses the TE_{00} guided mode, which on X-cut TFLN has large electro-optic coupling to fields parallel to both the chip surface and the crystal Z axis. Electrodes fabricated across each racetrack enable independent DC bias tuning of the uncoupled or *bare* mode frequencies via the linear electro-optic effect.²⁴ This is necessary to counteract drift and fabrication disorder.

We set the desired operating point by using the DC bias to tune all of the bare mode frequencies to be equal, which yields three evenly spaced resonances in the coupled or *dressed* basis with frequencies ω_i . In an ideal system, the spacing is $\Omega = \sqrt{2}\mu$ with $\mu \equiv |\mu_{12}| = |\mu_{23}|$. These three resonances couple to the bus waveguide through their spatial overlaps with the first racetrack and therefore lead to dips in the transmission spectrum, as shown in Fig. 1d. This overlap also means that RF modulation of the racetrack adjacent to the bus waveguide couples all three resonances together, as depicted by the schematic three-level system in Fig. 1d.

We apply an RF modulation of the form:

$$V(t) = A_1 \cos(\Omega t + \phi_1) + A_2 \cos(2\Omega t + \phi_2). \quad (1)$$

The frequency Ω corresponds to the microwave modulation frequency. In an ideal system with equal intermodal couplings μ , we would set Ω to $\sqrt{2}\mu$. Fabrication disorder and tuning imprecision means that the μ_{ij} 's are slightly different. For example, $\mu_{12}/2\pi = 1.864$ GHz and $\mu_{23}/2\pi = 1.861$ GHz, as inferred for the data in Fig. 1d, so we drive at $\Omega/2\pi = 2.63$ GHz, the average of the difference between the measured coupled resonance frequencies $\omega_1 - \omega_2$ and $\omega_2 - \omega_3$. Driving at Ω scatters light

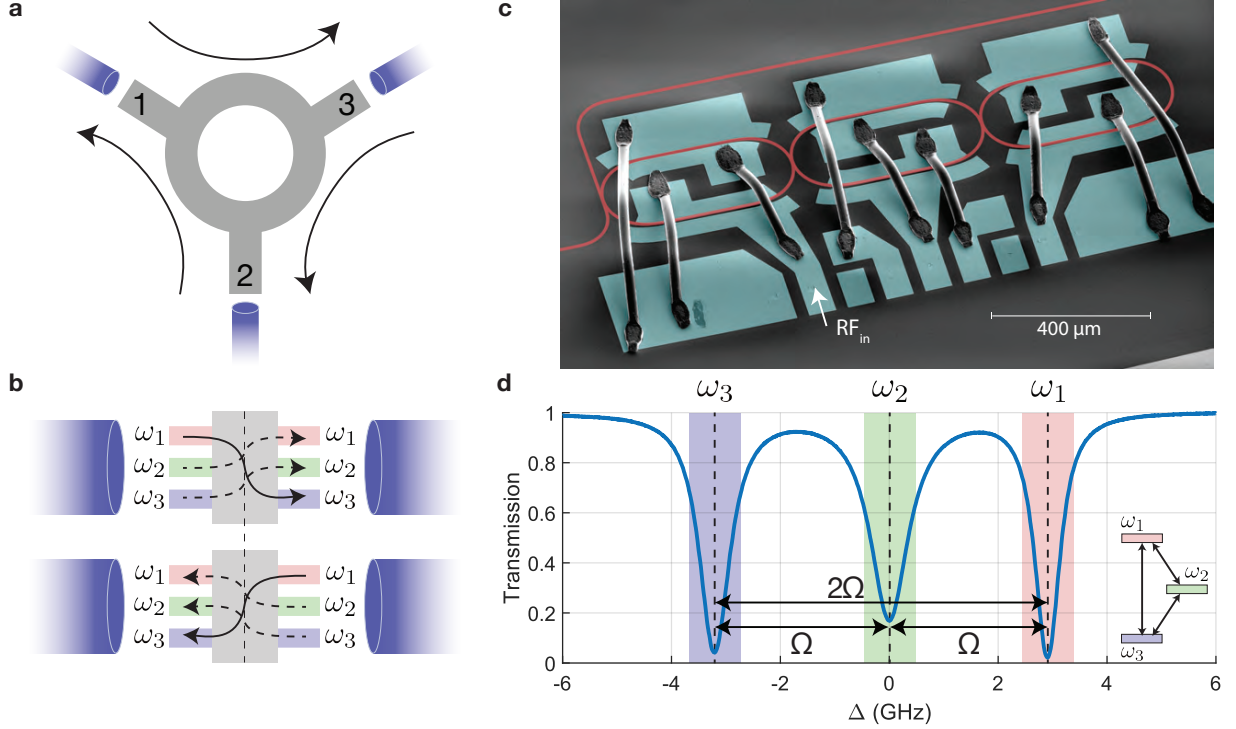


FIG. 1. Device structure and resonant system. (a) Schematic of a circulator consisting of three physical waveguide inputs/outputs. (b) Schematic of a circulator in frequency space operating within a single waveguide. The circulator can operate equivalently by inputting light from the left-side waveguide (top) or from the right-side waveguide (bot). The solid arrows emphasize the conversion from ω_1 to ω_3 , the dashed arrows indicate alternative frequency conversions, and the vertical dashed line depicts the structural mirror plane of the device. (c) SEM image (false-colored) of an identical device to that used in this experiment. Modulation is applied across both straight-lengths of the first (leftmost) racetrack. DC tuning is applied to the electrodes across the second (middle) racetrack. Lithium niobate (red) and gold electrodes (blue). (d) Optical spectrum of the hybridized super-modes of the device operating at 1543 nm. (d, inset) Schematic of the three-level system formed by the hybridized modes. Frequency conversion between any two modes can occur by two possible pathways; one path is a direct transition, and the other occurs in two steps, mediated by the third level.

between dressed modes ω_1 and ω_2 , whereas the 2Ω drive scatters light between modes ω_1 and ω_3 . For any pair of dressed modes, two possible transition pathways exist, as depicted by the schematic inset in Fig. 1d. One pathway is a direct transition, whereas the other is a two-step transition through the third mode. By varying the amplitudes and relative phases of the two RF tones, we enhance or suppress different pathways by generating interference. In the ideal disorder-free model, forward isolation (mode $\omega_1 \rightarrow \omega_3$) is maximized for the phase condition $2\phi_1 - \phi_2 = \pi/2$.

We characterize the performance of our circulator by measuring the scattering parameters S_{ij} , which quantify how the amplitude a_j of each incoming wave at frequency ω_j is converted to the amplitude of an outgoing wave b_i at frequency ω_i , propagating in the same direction in the opposite waveguide. This is depicted in Fig. 2a. We define an *isolation parameter* as

$$I_{ij} \equiv |S_{ij}|^2 / |S_{ji}|^2.$$

This characterizes the asymmetry between forward and backward frequency conversion for a pair of modes. As

shown in Fig. 2b for channels 1 and 3, it is clear that forward scattering from $1 \rightarrow 3$ occurs efficiently while the backward scattering is strongly suppressed. This leads to I_{31} approaching 40 dB when the driving phase condition is $\pi/2$ and A_i are correctly tuned, as explained below. Similar isolation is observed for other pairs of channels.

We obtain the scattering and isolation parameters described above by first characterizing the device's linear spectrum, with the RF modulation turned off. We measure the optical transmission parameter $t(\omega)|_{\text{RF,off}}$ as a function of frequency, which we then use to infer and DC-tune the device's parameters. This transmission amplitude evaluated at frequencies ω_j corresponds to $S_{jj}|_{\text{RF,off}}$ since it describes transmission through the device without a change in frequency. We place a laser tone at frequency ω_0 , blue-detuned from all of the resonances, and feed it through a commercial electro-optic modulator (EOM) before sending it to the device. Driving the EOM with a vector network analyzer (VNA), we generate two sidebands at $\omega_0 \pm \Delta$. By sweeping the VNA modulation frequency, we move one sideband across the cavity response, which then beats against the optical feed-

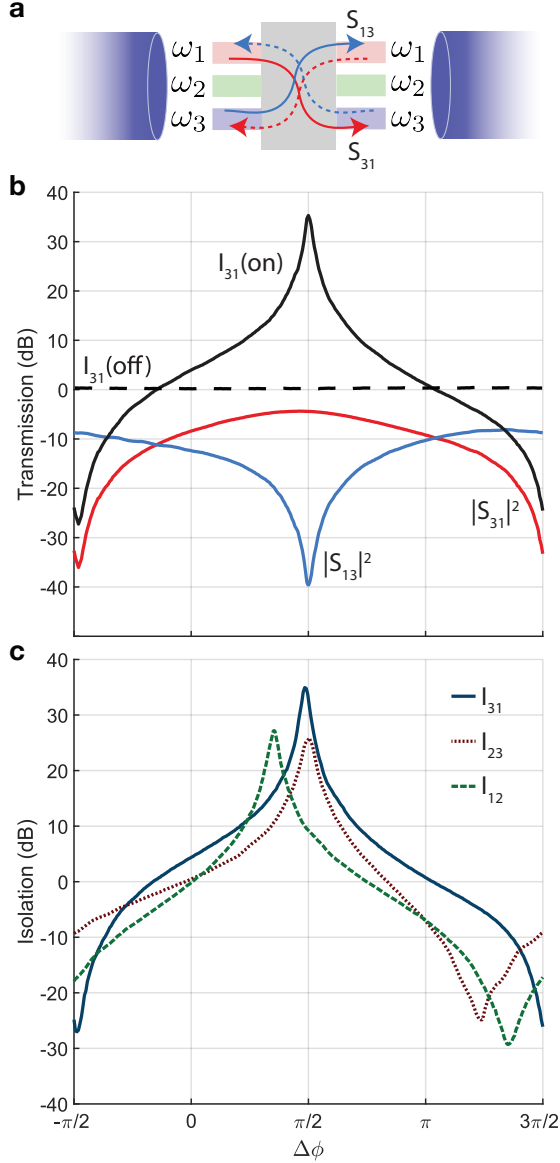


FIG. 2. **Isolation versus microwave phase condition**, $\Delta\phi = 2\phi_1 - \phi_2$. (a) Schematic of frequency-domain circulator. Solid arrows indicate light input from the waveguide on the left (as measured), and dashed arrows indicate the same conversions when light is input from the waveguide on the right. (b) Isolation for $\omega_1 \rightarrow \omega_3$ conversion. The line labeled “off” corresponds to decreasing the Ω frequency RF drive (P_1) while keeping the 2Ω drive (P_2) high, indicating the importance of coherent interference of the two processes for nonreciprocity. $P_1 = 73.2$ mW, $P_2 = 59.0$ mW. (c) Mutual isolation for all conversions observed for the fixed power condition in (b). Shifts between the peaks and the ideal phase condition stem from disorder in the mode hybridization.

through, ω_0 , on a subsequent RF photodiode connected to the VNA. Sweeping the VNA frequency allows us to see, nearly in real-time, the hybridized mode structure of the device, as shown in Fig. 3b. Our device exhibits DC bias drift as a result of photorefraction, a common

challenge in lithium niobate devices.^{25–27} This measurement technique enables us to observe and compensate for these changes as the optical input power and DC bias both affect the spectrum. We fit a complete model of the measurement, including the EOM transmission, cavity response, and phase response measured by the VNA in order to determine all of the device’s optical parameters (loss rates, resonant frequencies, etc.). An example of such a fit is depicted in Fig. 3c. We can also extract the sideband transmission $t(\omega)|_{\text{RF,off}}$ from these spectra.

We then measure the “active” device by turning on the RF drive and characterizing the scattering between frequency channels. Since VNA measurements only find linear scattering parameters, characterizing the scattering between frequencies requires a different measurement scheme than that described above. Keeping the laser at ω_0 , we modulate the EOM at frequency Δ in order to generate and input light at frequency $\omega_j = \omega_0 - \Delta$. We infer all of the optical powers in the different channels by making RF measurements of their beating against the feed-through light at ω_0 . This presents a minor complication for inferring S_{jj} , as the beat notes generated by both EOM sidebands $\omega_0 \pm \Delta$ interfere at RF frequency Δ . This ambiguity can be resolved by comparing measurements of S_{jj} to the independently measured scattering parameters (see previous paragraph) when RF modulation to the chip is turned *off*. Note that the other scattering parameters S_{ij} , $i \neq j$ can be inferred without this complication, so the isolation parameters I_{ij} are unaffected. For all scattering parameters, we record the RF power in the beat note corresponding to optical frequency ω_i , while varying the RF phase ϕ_2 . This power is proportional to $|b_i|^2$. We take the ratio of the measured power in ω_i to that of the unmodulated transmission at the signal frequency ω_j . By factoring out the contribution from the non-resonant input tone at $\omega_0 + \Delta$, we obtain the scattering parameters $|S_{ij}|^2 = |b_i/a_j|^2$ (see SI).

The scattering parameter measurements shown in Fig. 2 are taken for optimized values of the RF drive amplitude A_i . When the Ω RF drive is turned down, *i.e.*, $A_1 \approx 0$, but the 2Ω drive is kept on, we do not observe isolation (dashed line in Fig. 2b). For tuned values of A_1 and A_2 , we observe simultaneous isolation between the three pairs of dressed frequencies, demonstrating circulator-like behavior, as depicted in Fig. 2c.

We next characterize the RF power-dependent operation of our device by varying the modulation amplitudes A_1 and A_2 . For each power combination, we sweep the phase condition of the RF sources through multiple periods and extract the peak isolation observed for each transition. We generate maps of the isolation versus RF power, depicted in Fig. 4a-c. Each pixel is normalized by linear scattering parameters, analogously to the data in Fig. 2. The optical device characteristics used for this normalization are extracted from the VNA trace in Fig. 3, taken prior to varying the RF power.

Figures 4d-f depict theoretical plots of device performance obtained from coupled mode theory and show

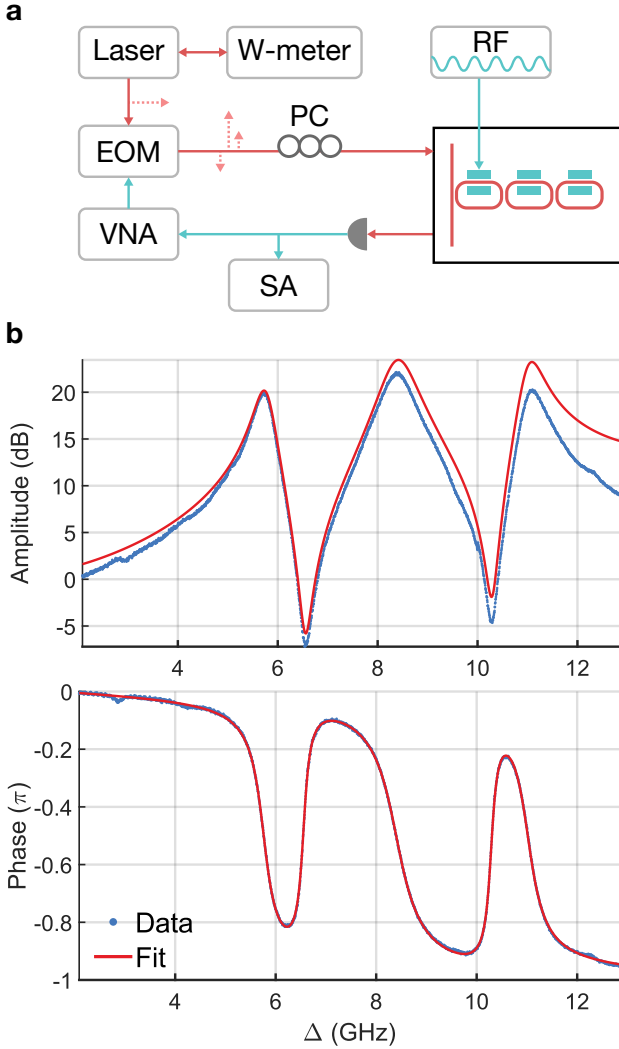


FIG. 3. **Experiment characterization scheme.** (a) Schematic of the characterization setup. (b) Background-normalized amplitude and phase of the VNA spectrum produced by the EOM response filtered through the optical cavity. The EOM is set to an approximately π DC phase shift. The fit is made to the phase response and used to predict the amplitude response.

good agreement with the measured trends. We attribute differences between theory and experiment, such as the slopes in the I_{31} maps and the locations of peak isolation in I_{12} and I_{23} , to mode drifts over the full course of measurement. This drift could emerge from either DC bias drift, which introduces disorder in the mode hybridization, or from high-power RF-induced drift (see SI). We assume this drift does not significantly affect the normalization factor we use for data processing, which is obtained from the initial VNA trace. From the theoretical plots, we infer a high-frequency bare mode modulation rate $g_{\text{EO}}/2\pi \approx 330$ MHz. This rate closely matches the directly measured low-frequency modulation rate $g_{\text{EO,DC}}/2\pi = 328.5$ MHz.

We can understand the trends in the isolation factor RF power dependence by studying the coupled mode theory description of the dynamics.¹ The RF modulation scatters photons between the dressed modes at a rate proportional to $\tilde{A}_i = g_{\text{EO}}A_i$, where g_{EO} is the electro-optic tuning of the bare RF-coupled mode. We observe strong enhancement in I_{31} in Fig. 4a,d along a locus corresponding to $\tilde{A}_1^2 \propto \tilde{A}_2$. This condition is found by noting that for cancellation to occur, the rate at which direct $1 \rightarrow 3$ scattering occurs, \tilde{A}_2 , needs to match the rate of indirect scattering $1 \rightarrow 2 \rightarrow 3$, which is approximately \tilde{A}_1^2/γ_2 ²⁸. Here, γ_2 is the linewidth (full-width, half-max – FWHM) of the second dressed mode. A more detailed analysis¹ indicates that maximum I_{13} isolation is given by:

$$\tilde{A}_2 = \frac{\tilde{A}_1^2}{2\gamma_2},$$

where $\gamma_2 = (\kappa_1 + \kappa_3)/2$.

A similar line of reasoning explains the large isolation regions in Fig. 4b,c,e,f. For example, note that a peak I_{12} requires interference between two scattering processes – a direct process $1 \rightarrow 2$, occurring with a rate \tilde{A}_1 , and an indirect process $1 \rightarrow 3 \rightarrow 2$, occurring at a rate $\tilde{A}_1\tilde{A}_2/\gamma_3$. This interference is maximized when the rates are nearly equal. A more detailed coupled mode analysis confirms that the ideal condition $\tilde{A}_2\tilde{A}_1 = 4\gamma_{1,3}\tilde{A}_1$, where $\gamma_{1,3} = (\kappa_1 + 2\kappa_2 + \kappa_3)/4$, maximizes the isolation parameter. The isolation parameters I_{12} and I_{23} are therefore maximized when:

$$\tilde{A}_2 = 4\gamma_{1,3},$$

independently of the direct scattering rate \tilde{A}_1 . Inhomogeneity in the mode hybridization causes deviations from this exact condition for I_{23} versus I_{12} , *i.e.*, they appear at slightly different power conditions in Fig. 4b,c.

Discussion

Our platform's most significant limit is due to optical loss in the cavities. In the ideal realization the dressed mode linewidths are entirely due to coupling out into the feed waveguide. When the RF drives are off, the absence of intrinsic loss means that the dressed modes are over-coupled, so $|S_{kk}| = 1$. As we increase the RF driving power, the scattering between dressed modes appears as additional loss at the signal frequency. This moves the mode from being over-coupled into a critically coupled condition, when the scattering-induced loss at mode k equals the mode's coupling rate to the waveguide and leads to $|S_{kk}| = 0$. However, in the experimentally realized system, there is additional intrinsic loss in all three cavities, and the dressed modes are already close to being critically coupled when the RF drives are off. The RF induced scattering then acts to *increase* transmission $|S_{kk}|$ as it moves the mode farther away from being critically coupled. This means that in contrast to the ideal circulator, the diagonal elements of the scattering matrix are

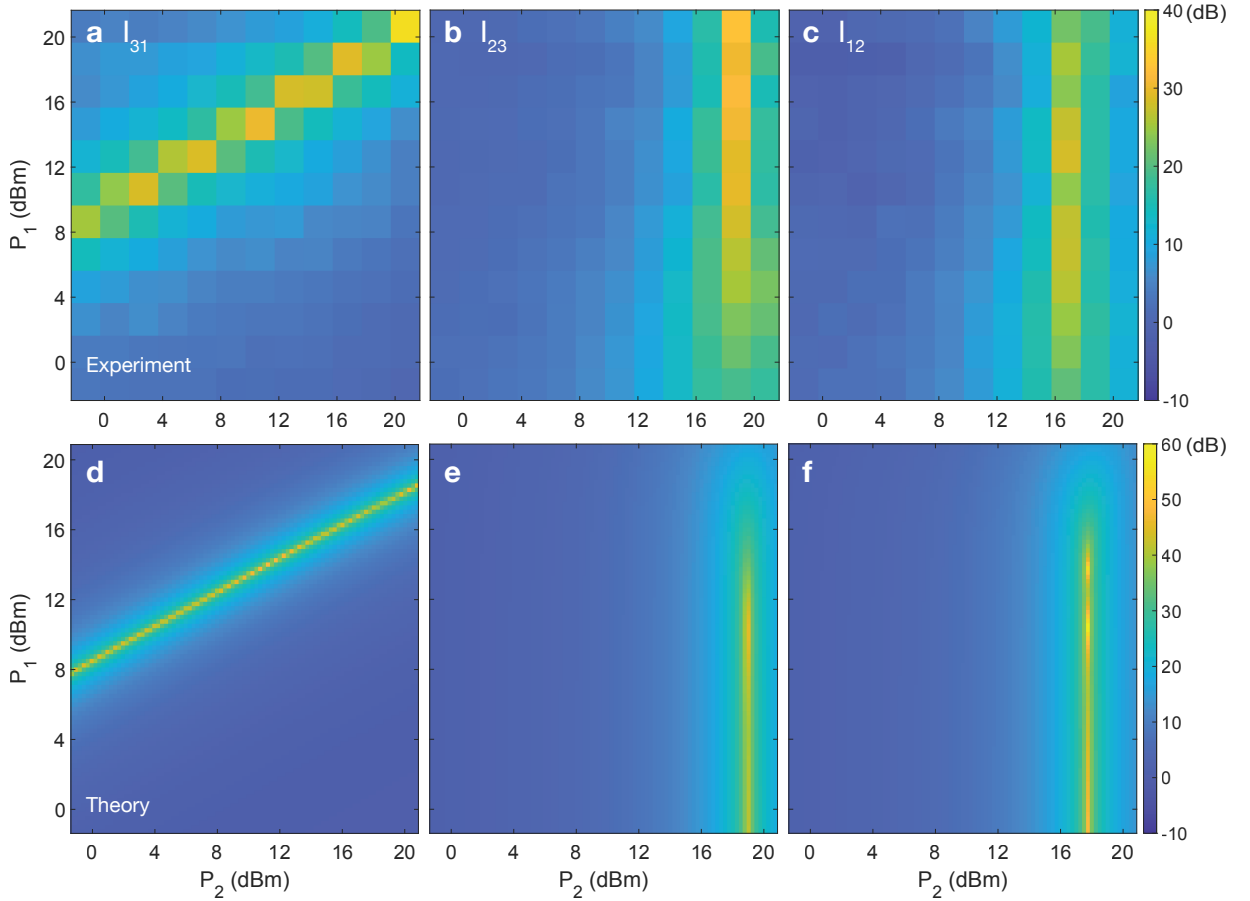


FIG. 4. **Isolation versus microwave power.** We sweep the two RF drive powers, indicated here as P_1 (Ω drive) and P_2 (2Ω drive). For each power combination, the phase of the 2Ω drive (ϕ_2) is swept across multiple periods. Each pixel corresponds to the maximum observed isolation for each RF power combination for a given isolation parameter. The phase condition varies between pixels of different maps. The top row corresponds to measurements, and the bottom row are theoretical predictions of isolation. We attribute differences between experiment and theory to shifting system parameters over time and as the RF power increases (see SI). Predictions are based on the fit system parameters, which also have some degree of uncertainty.

nonzero in our realization. We expect that with improvements in optical Q of on-chip LN devices, this problem can be largely eliminated.²⁹ One possible way to circumvent this challenge in the shorter term is to include an additional resonator after the device at frequency ω_k in order to filter out any feed-through and make $S_{kk} = 0$ for a single channel. Another approach that does not require major improvements in the Q is to increase the cavity-waveguide coupling and start within a more over-coupled regime. However, this approach would require larger RF powers and we are already power-limited. The off-chip microwave amplifier saturates at approximately 35 dBm. Moreover, as power to the device increases above roughly 120 mW, we observe dressed mode drifts on the order of MHz, which disrupts the resonance condition required for high isolation (see SI).

Another limit of our approach is due to its resonant nature. The isolation bandwidth of our device depends on the dressed mode linewidths, and we measured sustained isolation over more than a few hundred megahertz.

This too can be increased, but at the cost of greater RF power as the \tilde{A}_k also scale with bandwidth. One strategy to make the modulation more efficient would be to include modulation into the third racetrack. Alternatively, since we only need narrowband RF modulation, we could use the extremely efficient optomechanical modulation schemes recently demonstrated on LN^{30–32} to significantly reduce the needed RF power and realize larger bandwidth. Finally, we note that the bandwidth of the device is potentially larger than the linewidth of a single mode as there are families of modes repeating with the cavity free spectral range, and under low disorder, these would also behave as circulators for signals at different sets of frequencies.

A novel feature of our device is its operation as a *bi-directional* isolator – a property that emerges from mirror symmetry and frequency-domain operation. For example, two transmitters/receivers can operate simultaneously along a single channel. Node 1 can transmit a signal down a waveguide at frequency ω_1 to node 2, who

receives at ω_3 . This communication is isolated. Meanwhile, node 2 can then send a signal backwards along the waveguide at ω_1 to node 1, who also receives at ω_3 . This communication is also isolated. With the standard optical isolator, this behavior would require two optical channels, one for each direction of transmission.

Overall, we have demonstrated an integrated frequency isolator/circulator on thin-film lithium niobate, an emerging platform for classical and quantum photonics. We measured peak isolation of nearly 40 dB with 4.4 dB insertion loss for dual RF drive powers of $P_1 = 73.2$ mW $P_2 = 59.0$ mW. Our device is reconfigurable, enabling isolation over a wide range of powers for different operating frequencies. For example, we also measure $\omega_1 \rightarrow \omega_3$ isolation of more than 25 dB for dual RF powers of $P_1 = 7.32$ mW and $P_2 = 0.74$ mW, but with a commensurate increase of insertion loss (~ 16 dB). Furthermore, we also measured insertion loss as low as 3 dB for different power and isolation conditions. Ultimately, the mirror symmetry and frequency-domain operation of our device provide for novel applications as an isolator/circulator and frequency router in photonic circuits.

Methods

Fabrication. The device is fabricated in a two-mask process from 500 nm-thick film of lithium niobate (LN) atop a sapphire (Sa) handle. The components are air-clad, and the electrodes are fabricated as a Ti:Au metal bilayer. The first mask, for photonics fabrication, is defined from hydrogen silsequioxane (HSQ), a negative-tone electron beam resist, patterned with 100 kV electron beam lithography (JEOL JBX-6300FS). We transfer the patterns into the LN with argon ion mill etching (IntiVac ion mill), followed by an acid cleaning procedure. We confirm the device's optical performance prior to fabricating electrodes. The electrodes are defined with a standard photoresist lift-off bilayer. The patterns are written using direct-write lithography (Heidelberg MLA150), and metal is evaporated (Kurt J. Lesker LAB18) prior to solvent-based liftoff. Lastly, we wirebond on-chip to connect electrodes across the optics, thereby defining proper modulation polarity on-chip (West Bond 7476E).

Characterization. The device is optically pumped from a telecommunications wavelength diode laser (Santec TSL-550). We lock the optical pump blue-detuned from the modes at 1543.6 nm (via a Bristol Wavemeter). The light is passed through a polarization control wheel and in-line fiber polarizer to maximize TE transmission. This light is passed into a commercial electro-optic amplitude modulator (EOM). We drive the EOM from a VNA (R&S ZNB20) in order to generate sidebands. The pump and sidebands are then passed through another polarization controller, into a variable optical attenuator (VOA), then a power meter before being passed onto the chip. By sweeping the frequency of the VNA output (or by driving a particular frequency) we can sweep the sideband across (or directly drive) the optical dressed modes of the

system. The light undergoes modulation on-chip. Output light from the optical waveguide passes through an erbium-doped fiber amplifier (EDFA) and an X-switch, which switches our detector between a photodiode for linear optical characterization, and a fast photo-diode (Optilab PD-40M), which records beat tones between the optical pump, the EOM sideband, and converted sidebands when applying on-chip modulation. The output of the fast photodiode passes through a bias-tee. One arm passes back to the VNA to record the broad-band response of the cavity, and the other arm passes to a spectrum analyzer (R&S FSW26) to record converted sideband powers with high precision. This setup enables us to simultaneously observe the full cavity response on the VNA in nearly real-time while adjusting DC bias across the device and manipulating the optical pump, while also observing sideband powers at particular frequencies when driving on-chip modulation.

In order to characterize our device mirror symmetry, we separately insert a second X-switch and polarization control just before the device. We record transmission through the device from both waveguide propagation directions, demonstrating equivalence of scattering matrix elements (see SI).

On-chip modulation is driven from two pulsed signal generators (PSG, Keysight E8257D). One PSG drives the Ω tone while the other drives the 2Ω tone. We vary the relative phase between these sources. The clocks of the PSGs are locked together, and these are in turn locked to the clock of the FSW26. The two PSG outputs are combined at a power splitter and passed through a high-power microwave amplifier. The output of the amplifier is then passed to a probe, which is contacted to the on-chip electrical pads. Importantly, the rate of direct phase modulation on the PSG is much faster than the global phase drift of the system, enabling us to visualize power modulations at sideband frequencies on the FSW26.

Author contribution. J.F.H. fabricated the device. J.F.H. and V.A. led the experimental effort. J.W. developed the device operating theory and characterized theoretical device performance. J.F.H., J.D.W., and J.W. determined physical device designs. J.D.W. assisted in early experimentation. A.H.S.N and S.F. provided experimental and theoretical guidance and support for this experiment.

Acknowledgements

J.F.H. acknowledges support from the National Science Foundation Graduate Research Fellowship Program (Grant No. DGE-1656518). V.A. acknowledges support by the Stanford Q-FARM Bloch Fellowship Program. The authors acknowledge the support of an AFOSR MURI project (FA9550-18-1-0379), the National Science Foundation under award ECCS-1820938, and the Defense Advanced Research Projects Agency (DARPA) LUMOS program. Part of this work was performed at the Stanford Nano Shared Facilities (SNSF), supported by the National Science Foundation under award ECCS-2026822. Work was performed in part in the nano@stanford labs, which are supported by the National Science Foundation as part of the National Nanotechnology Coordinated Infrastructure under award ECCS-1542152. The authors would like to thank Wentao Jiang and Christopher J. Sarabalis for insightful and helpful discussions.

* jfherm@stanford.edu

¹ J. Wang, J. F. Herrmann, J. D. Witmer, A. H. Safavi-Naeini, and S. Fan, *Phys. Rev. Lett.* **126**, 193901 (2021).
² L. Bi, J. Hu, P. Jiang, D. H. Kim, G. F. Dionne, L. C.

Kimerling, and C. Ross, *Nature Photonics* **5**, 758 (2011).
³ L. D. Tzuang, K. Fang, P. Nussenzeig, S. Fan, and M. Lipson, *Nature photonics* **8**, 701 (2014).
⁴ K. Srinivasan and B. J. Stadler, *Optical Materials Express*

- 8, 3307 (2018).
- ⁵ D. Huang, P. Pintus, C. Zhang, Y. Shoji, T. Mizumoto, and J. E. Bowers, *IEEE Journal of Selected Topics in Quantum Electronics* **22**, 271 (2016).
- ⁶ W. Yan, Y. Yang, S. Liu, Y. Zhang, S. Xia, T. Kang, W. Yang, J. Qin, L. Deng, and L. Bi, *Optica* **7**, 1555 (2020).
- ⁷ Y. Sobu, Y. Shoji, K. Sakurai, and T. Mizumoto, *Opt. Express* **21**, 15373 (2013).
- ⁸ E. A. Kittlaus, N. T. Otterstrom, P. Kharel, S. Gertler, and P. T. Rakich, *Nature Photonics* **12**, 613 (2018).
- ⁹ E. A. Kittlaus, W. M. Jones, P. T. Rakich, N. T. Otterstrom, R. E. Muller, and M. Rais-Zadeh, *Nature Photonics* **15**, 43 (2021).
- ¹⁰ S. Kim, D. B. Sohn, C. W. Peterson, and G. Bahl, *APL Photonics* **6**, 011301 (2021).
- ¹¹ Z. Shen, Y.-L. Zhang, Y. Chen, C.-L. Zou, Y.-F. Xiao, X.-B. Zou, F.-W. Sun, G.-C. Guo, and C.-H. Dong, *Nature Photonics* **10**, 657 (2016).
- ¹² F. Ruesink, M.-A. Miri, A. Alu, and E. Verhagen, *Nature communications* **7**, 1 (2016).
- ¹³ M. S. Kang, A. Butsch, and P. S. J. Russell, *Nature Photonics* **5**, 549 (2011).
- ¹⁴ J. Kim, M. C. Kuzyk, K. Han, H. Wang, and G. Bahl, *Nature Physics* **11**, 275 (2015).
- ¹⁵ C.-H. Dong, Z. Shen, C.-L. Zou, Y.-L. Zhang, W. Fu, and G.-C. Guo, *Nature communications* **6**, 1 (2015).
- ¹⁶ M. Hafezi and P. Rabl, *Optics express* **20**, 7672 (2012).
- ¹⁷ H. Tian, J. Liu, A. Siddharth, R. N. Wang, T. Blésin, J. He, T. J. Kippenberg, and S. A. Bhawe, *arXiv preprint arXiv:2104.01158* (2021).
- ¹⁸ D. Sohn, O. E. Örsel, and G. Bahl, *arXiv preprint arXiv:2104.04803* (2021).
- ¹⁹ K. Fang, Z. Yu, and S. Fan, *Physical review letters* **108**, 153901 (2012).
- ²⁰ H. Lira, Z. Yu, S. Fan, and M. Lipson, *Physical review letters* **109**, 033901 (2012).
- ²¹ C. R. Doerr, N. Dupuis, and L. Zhang, *Optics letters* **36**, 4293 (2011).
- ²² Z. Yu and S. Fan, *Nature Photonics* **3**, 91 (2009).
- ²³ N. Dostart, H. Gevorgyan, D. Onural, and M. A. Popović, *Optics Letters* **46**, 460 (2021).
- ²⁴ R. S. Weis and T. K. Gaylord, *Applied Physics A.* , 191 (1985).
- ²⁵ T. P. McKenna, J. D. Witmer, R. N. Patel, W. Jiang, R. van Laer, P. Arrangoiz-Arriola, E. A. Wollack, J. F. Herrmann, and A. H. Safavi-Naeini, *Optica* **7**, 1737 (2020).
- ²⁶ H. Jiang, R. Luo, H. Liang, X. Chen, Y. Chen, and Q. Lin, *Opt. Lett.* **42**, 3267 (2017).
- ²⁷ Y. Xu, M. Shen, J. Lu, J. B. Surya, A. A. Sayem, and H. X. Tang, *Opt. Express* **29**, 5497 (2021).
- ²⁸ By second-order perturbation theory.
- ²⁹ A. Shams-Ansari, G. Huang, L. He, M. Churaev, P. Kharel, Z. Tan, J. Holzgrafe, R. Cheng, D. Zhu, J. Liu, B. Desiatov, M. Zhang, T. J. Kippenberg, and M. Lončar, in *Conference on Lasers and Electro-Optics* (Optical Society of America, 2021) p. STh4J.4.
- ³⁰ W. Jiang, C. J. Sarabalis, Y. D. Dahmani, R. N. Patel, F. M. Mayor, T. P. McKenna, and R. van Laer and Amir H. Safavi-Naeini, *Nature Communications* **1166** (2020), <https://doi.org/10.1038/s41467-020-14863-3>.
- ³¹ L. Shao, M. Yu, S. Maity, N. Sinclair, L. Zheng, C. Chia, A. Shams-Ansari, C. Wang, M. Zhang, K. Lai, and M. Lončar, *Optica* **6**, 1498 (2019).
- ³² C. J. Sarabalis, T. P. McKenna, R. N. Patel, R. Van Laer, and A. H. Safavi-Naeini, *APL Photonics* **5**, 086104 (2020), <https://doi.org/10.1063/5.0012288>.
- ³³ R. N. Patel, Z. Wang, W. Jiang, C. J. Sarabalis, J. T. Hill, and A. H. Safavi-Naeini, *Phys. Rev. Lett.* **121**, 040501 (2018).
- ³⁴ I. A. Williamson, M. Minkov, A. Dutt, J. Wang, A. Y. Song, and S. Fan, *Proceedings of the IEEE* **108**, 1759 (2020).
- ³⁵ W. Jiang, C. J. Sarabalis, Y. D. Dahmani, R. N. Patel, F. M. Mayor, T. P. McKenna, R. Van Laer, and A. H. Safavi-Naeini, *Nature Communications* **11**, 1166 (2020).

Supplementary Information: Mirror symmetric on-chip frequency circulation of light

S1. FITTING EOM RESPONSE

A. Cavity Response and Coupled Eigenmodes

We derive the cavity response in the bare-mode basis according to standard coupled mode theory. In the following, κ_i describes the total decay rate of bare mode i , μ_{ij} is the coupling between bare modes i and j , and κ_e is the extrinsic coupling rate of the first ring coupled to the waveguide ($\kappa_1 = \kappa_{1,i} + \kappa_e$). The triple-ring system is described by the Hamiltonian:

$$H = H_0 + H_{int} + H_{WG}$$

- $H_0 = \hbar \left(\omega_{0,1} \hat{a}_1^\dagger \hat{a}_1 + \omega_{0,2} \hat{a}_2^\dagger \hat{a}_2 + \omega_{0,3} \hat{a}_3^\dagger \hat{a}_3 \right)$
- $H_{int} = \hbar \sum_{i < j} \mu_{ij} \left(\hat{a}_i^\dagger \hat{a}_j + \hat{a}_j^\dagger \hat{a}_i \right) + H_{WG-int}$
- $H_{WG} = -\hbar \int d\omega \gamma(\omega) \hat{b}^\dagger(\omega) \hat{b}(\omega)$

We take the Heisenberg equations of motion to arrive at the coupled mode theory for the three resonances, \hat{a}_i :

$$\dot{\hat{a}}_1(t) = - \left(i\omega_{0,1} + \frac{\kappa_1}{2} \right) \hat{a}_1 - i\mu_{12} \hat{a}_2 - \sqrt{\kappa_e} b_{in} \quad (1a)$$

$$\dot{\hat{a}}_2(t) = - \left(i\omega_{0,2} + \frac{\kappa_2}{2} \right) \hat{a}_2 - i\mu_{12} \hat{a}_1 - i\mu_{23} \hat{a}_3 \quad (1b)$$

$$\dot{\hat{a}}_3(t) = - \left(i\omega_{0,3} + \frac{\kappa_3}{2} \right) \hat{a}_3 - i\mu_{23} \hat{a}_2 \quad (1c)$$

$$b_{out} = b_{in} + \sqrt{\kappa_e} \hat{a}_1(t) \quad (1d)$$

We go into a frame rotating with the laser frequency, ω_0 . This shifts our resonances relative to the drive tone, $\omega_{0,i} \rightarrow \Delta_i = \omega_{0,i} - \omega_0$. Fourier transforming into the frequency domain and taking $b_{in} = 0$, we obtain the eigenvalue equation 2.

$$\begin{pmatrix} -\left(i\Delta_1 + \frac{\kappa_1}{2}\right) & -i\mu_{12} & 0 \\ -i\mu_{12} & -\left(i\Delta_2 + \frac{\kappa_2}{2}\right) & -i\mu_{23} \\ 0 & -i\mu_{23} & -\left(i\Delta_3 + \frac{\kappa_3}{2}\right) \end{pmatrix} \vec{a} = -i\omega \vec{a} \quad (2)$$

Here, $\vec{a} = (\hat{a}_1, \hat{a}_2, \hat{a}_3)^T$. The real part of the eigenvalues corresponds to the dressed mode frequencies ω_i , and the dressed mode loss rates are twice the magnitude of the imaginary part.

Taking the Fourier Transform of the equations of motion has the effect of the following further substitutions:

$$\begin{aligned} \Delta_i &\rightarrow \Delta'_i = \Delta_i - \Omega \\ \Rightarrow 0 &= - \left(i\Delta'_1 + \frac{\kappa_1}{2} \right) \hat{a}_1(\Omega) - i\mu_{12} \hat{a}_2(\Omega) - \sqrt{\kappa_e} b_{in}(\Omega) \end{aligned}$$

(and similarly for modes 2,3). We solve the Fourier transformed equations 1 for the linear cavity transmission in the frame rotating with the laser:

$$t(\Omega) = \frac{b_{out}}{b_{in}} = 1 - \frac{\kappa_e}{i\Delta'_1 + \frac{\kappa_1}{2} + \frac{\mu_{12}^2}{i\Delta'_2 + \frac{\kappa_2}{2} + \frac{\mu_{23}^2}{i\Delta'_3 + \frac{\kappa_3}{2}}}} \quad (3)$$

B. EOM Response

We calculate the photodiode response to light modulated by an EOM traveling through our device.³³ An intensity modulator can be described as a 50/50 beam-splitter, followed by a variable phase shift on one path, followed by a

second 50/50 beam-splitter. This is given by the following.

$$(\alpha_{\text{out}}, \cdot)^T = \frac{1}{2} \begin{pmatrix} 1 & i \\ i & 1 \end{pmatrix} \begin{pmatrix} b & 0 \\ 0 & ae^{i\phi} \end{pmatrix} \begin{pmatrix} 1 & i \\ i & 1 \end{pmatrix} (\alpha_{\text{in}}, 0)^T \quad (4)$$

In the above, $(\alpha_{\text{in}}, 0)^T$ is the laser input in the rotating frame of the laser. Furthermore, b, a describe asymmetric loss between the arms of the integrated modulator. The phase accumulated in the EOM is given by a DC phase shift, θ , plus harmonic modulation:

$$\phi = \theta + \beta \cos(\Omega t + \phi') \quad (5)$$

β is small, so we can neglect higher-order sidebands. We solve for the time-dependent transmission through the EOM:

$$\alpha_{\text{out}} = \frac{\alpha_{\text{in}}}{2} \left[(b - ae^{i\theta}) - \frac{i\beta}{2} e^{i\theta} e^{i\phi'} e^{i\Omega t} - \frac{i\beta}{2} e^{i\theta} e^{-i\phi'} e^{-i\Omega t} \right] \quad (6)$$

In our experiment, the laser is blue-detuned from the cavity, so the $-|\Omega|$ sideband sweeps across a mode as we sweep the modulation frequency Ω . The carrier and both sidebands are then filtered by the linear cavity response in eq. 3 to yield the time-dependent transmission through our device. This leads to an output field amplitude:

$$\alpha_{\text{out}} = \frac{\alpha_{\text{in}}}{2} \left[(a - e^{i\theta})t(0) - \frac{i\beta}{2} e^{i\theta} e^{i\phi'} e^{i\Omega t} t(-\Omega) - \frac{i\beta}{2} e^{i\theta} e^{-i\phi'} e^{-i\Omega t} t(+\Omega) \right] \quad (7)$$

This transmitted field is recorded on a photodiode and routed to a VNA. We AC-couple the output to neglect DC offsets:

$$\begin{aligned} |\alpha_{\text{out}}|^2 &= \frac{i|\alpha_{\text{in}}|^2\beta}{8} e^{i\phi'} e^{i\Omega t} [(a - e^{i\theta})e^{-i\theta} t(0)t^*(+\Omega) - (a - e^{-i\theta})e^{i\theta} t^*(0)t(-\Omega)] + c.c. \\ &= Z(\Omega)e^{i\Omega t} + Z^*(\Omega)e^{-i\Omega t} \end{aligned} \quad (8)$$

The voltage from the photodiode is given by $V(t) \sim \mathcal{R}\{Z(\Omega)e^{i\Omega t}\}$, and the VNA trace is proportional to the amplitude of the complex number $Z(\Omega)$.

We normalize by the far-detuned response ($t(\omega) = t(0) \approx 1, \Delta \gg 1$), which allows us to cancel pre-factors corresponding to the carrier tone amplitude, RF modulation amplitude, global phases, and frequency-dependent cable and detector losses. We can fit the normalized phase response of the VNA ($\arg\{Z(\Omega)\}$) to determine system parameters.

C. Bootstrapping: System Parameters

Our model has many free parameters, so our fit quality is sensitive to an initial guess. We account for this by applying a modified bootstrap algorithm. We repeatedly fit subsets of the VNA trace using random parameter guesses within physical bounds. We obtain distributions of the fit parameters, summarized in table S1B. After fitting $\Delta_1, \Delta_2, \Delta_3$, we can solve eq. 2 for the dressed mode detunings, ω_i , from the carrier tone. We generate input signals at dressed mode frequencies by driving the EOM at $|\omega_i|$. When the EOM DC bias phase $\theta \approx \pi$, the VNA trace appears symmetric, and we can approximate the super-mode locations by extracting the peaks in the VNA trace. In order to improve the symmetry of the mode transitions in the conversion experiment, we apply RF modulation at $\Omega = (\omega_1 - \omega_3)/2$, and we position the ω_2 input at $(\omega_1 + \Omega)/2\pi = 8.391$ GHz.

S2. SCATTERING MATRIX FORMALISM

A. Normalization and Scattering Parameters

In order to establish non-reciprocity, we must demonstrate that the scattering matrix describing input and output of the device is asymmetric.³⁴ We first consider the forward (left-to-right) propagating modes. In the main text, we describe our measurement procedure to obtain scattering matrix elements. We measure the linear transmission amplitude, corresponding to un-modulated signal light, a_j . The power recorded through the photodiode onto an FSW,

TABLE S1. System parameters, measured and fit to VNA phase trace

Parameter	Description	Average	95% Confidence Interval
ω_L	Wavelength of laser drive	1543.605 nm	-
$\kappa_e/2\pi$	Extrinsic loss rate of the first resonator	847 MHz	[711, 1002] MHz
$\kappa_i/2\pi$	Intrinsic loss rate of the first resonator	404 MHz	[249, 540] MHz
$\kappa_1/2\pi$	First resonator total loss rate ($\kappa_1 = \kappa_e + \kappa_i$)	1.251 GHz	[1.247, 1.254] GHz
$\kappa_2/2\pi$	Second resonator total loss rate	198 MHz	[196, 200] MHz
$\kappa_3/2\pi$	Third resonator total loss rate	225 MHz	[222, 228] MHz
$\mu_{12}/2\pi$	Coupling rate between first and second resonators	1.864 GHz	[1.863, 1.865] GHz
$\mu_{23}/2\pi$	Coupling rate between second and third resonators	1.861 GHz	[1.861, 1.862] GHz
$\Delta_1/2\pi$	Detuning of first bare mode from laser drive	-8.616 GHz	[-8.621, -8.611] GHz
$\Delta_2/2\pi$	Detuning of second bare mode from laser drive	-8.384 GHz	[-8.386, -8.383] GHz
$\Delta_3/2\pi$	Detuning of third bare mode from laser drive	-8.175 GHz	[-8.180, -8.170] GHz
$\omega_3/2\pi$	Detuning of third dressed mode from laser drive	-11.016 GHz	[-11.016, -11.015] GHz
$\omega_2/2\pi$	Detuning of second dressed mode from laser drive	-8.400 GHz	[-8.401, -8.399] GHz
$\omega_1/2\pi$	Detuning of first dressed mode from laser drive	-5.761 GHz	[-5.761, -5.760] GHz
$\Omega/2\pi$	RF drive frequency	2.63 GHz	-
P_1	RF power used in below detuning study	73.2 mW	-
P_2	RF power used in below detuning study	59.0 mW	-
$g_{\text{EO,RF}}/2\pi$	High frequency bare mode modulation rate (inferred)	330 MHz/V	-
$g_{\text{EO,DC}}/2\pi$	Low frequency bare mode modulation rate (measured)	328.5 MHz/V	-

\tilde{a}_j includes contributions from both the resonant EOM sideband (*i.e.*, the signal input at frequency $\omega_j = \omega_0 - \Delta$) and the non-resonant sideband ($\omega_0 + \Delta$). The measured power is related to the input signal amplitude by a normalization factor: $a_j = \eta_j \tilde{a}_j$. Turning on RF modulation, we measure the converted sideband amplitudes b_i . Scattering is given by the expression:

$$\vec{b}_i = \mathbf{S}_{ij} \vec{a}_j = \begin{pmatrix} S_{11} & S_{12} & S_{13} \\ S_{21} & S_{22} & S_{23} \\ S_{31} & S_{32} & S_{33} \end{pmatrix} \begin{pmatrix} \eta_1 \tilde{a}_1 \\ \eta_2 \tilde{a}_2 \\ \eta_3 \tilde{a}_3 \end{pmatrix} \quad (9)$$

The power in a given sideband is proportional to the integration of the autocorrelation function S_{VV} , which is recorded on the FSW. This integration is proportional to $|Z(\Omega)|^2$ from 8. We therefore measure sideband power as a function of the transmitted signal power:

$$|S_{ij}|^2 = \frac{|b_i|^2}{|Z(|\omega_j|)\eta(\omega_j)|^2} \propto \frac{|b_i|^2}{|(a - e^{i\theta})e^{-i\theta}t(0)t^*(|\omega_j|) - (a - e^{-i\theta})e^{i\theta}t^*(0)t(-|\omega_j|)|^2|\eta_j|^2} \quad (10)$$

We identify η_j such that we factor out the non-resonant sideband contribution in 10.

$$|\eta_j|^2 = \frac{|(a - e^{-i\theta})e^{i\theta}t^*(0)|^2}{|(a - e^{i\theta})e^{-i\theta}t(0)t^*(|\omega_j|) - (a - e^{-i\theta})e^{i\theta}t^*(0)t(-|\omega_j|)|^2} \quad (11)$$

All of the free parameters in equations 10 and 11 are obtained via the fits demonstrated in section S1 C. The diagonal elements S_{jj} also contain a non-resonant contribution in the transmitted power measurement, so they require a slightly modified normalization factor.

For a fixed phase condition, $\Delta\phi = 2\phi_1 - \phi_2$, and modulation amplitudes, $P_1 = 73.2$ mW and $P_2 = 59.0$ mW, the scattering matrix \mathbf{S} takes on an asymmetric form demonstrating circulation. The diagonal elements correspond to feedthrough at the original signal frequency as described in the main text. Here we present the scattering matrices for both forward ($1 \rightarrow 3 \rightarrow 2 \rightarrow 1$) and reverse ($1 \rightarrow 2 \rightarrow 3 \rightarrow 1$) circulation for left-to-right-propagating signals.

$$\Delta\phi = +\frac{\pi}{2} \implies |S_+|^2 = \begin{pmatrix} 0.21 & 0.21 & 0.00 \\ 0.02 & 0.19 & 0.26 \\ 0.36 & 0.00 & 0.29 \end{pmatrix} \quad (12)$$

$$\Delta\phi = -\frac{\pi}{2} \implies |S_-|^2 = \begin{pmatrix} 0.19 & 0.01 & 0.13 \\ 0.35 & 0.25 & 0.05 \\ 0.00 & 0.30 & 0.38 \end{pmatrix} \quad (13)$$

The scattering matrices are asymmetric, thereby demonstrating non-reciprocal frequency conversion and amplitude transmission between the frequency ports. Diagonal elements correspond to feed-through at the original signal frequencies, which can be reduced using techniques discussed in the main text.

B. Forward and Reverse Isolation

We confirm mirror symmetry in our device by measuring and comparing isolation for light propagating from left-to-right versus right-to-left in the feed waveguide. We insert an “x-switch” and additional polarization controller before the device in order to swap the waveguide input direction. We match polarization of the input light between the two paths and measure I_{31} , depicted in Fig. S5. Isolation is equivalent for light propagating from either direction in the bus waveguide. This validates our single-port characterization scheme. We attribute slight discrepancies between the propagation directions to fluctuations in the polarization on each path. This measurement was taken for RF drive powers $P_1 = 74.7$ mW and $P_2 = 65.6$ mW and for RF drive frequency $\Omega = 2.64$ GHz.

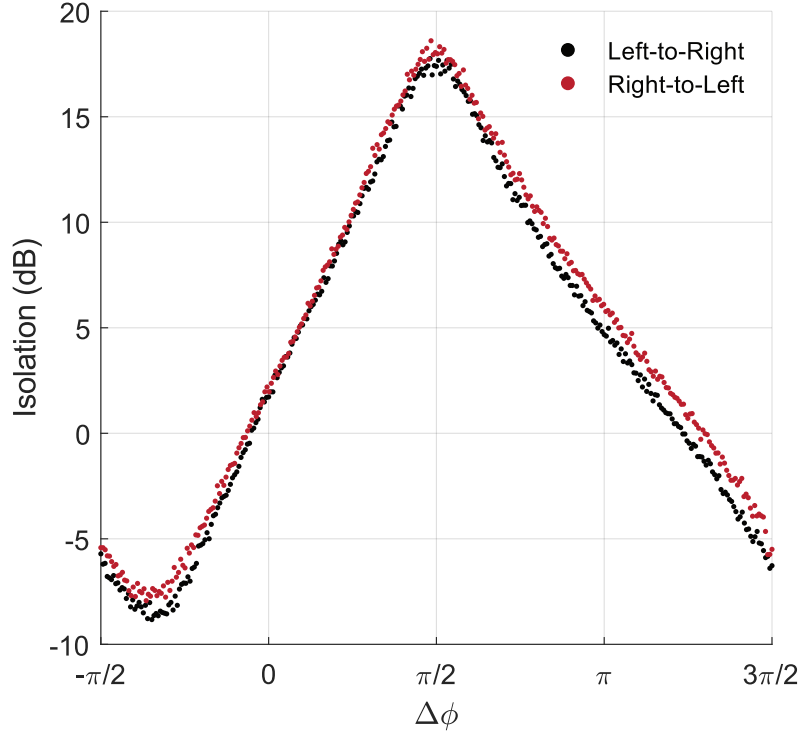


FIG. S5. **Mirror symmetric isolation, I_{31} .** Inputs propagating from left-to-right versus right-to-left in the bus waveguide yield equivalent sideband conversion and isolation. Fluctuations in the transmission and conversion are due to slight differences in the polarization of input light from either direction.

S3. PUMP DEPLETION

We characterize the effects of RF modulation on mode drift by applying RF modulation at $\Omega/2\pi = (\omega_1 - \omega_3)/2\pi = 5.26$ GHz and recording a series of spectra on the VNA. After collecting several traces, we turn off modulation and record another series of traces. By recording the time stamp of each scan, we measure mode drifts in near real-time.

Figure S7 presents scans taken at various RF powers. The black dashed line indicates the first scan for which modulation is turned off in each set. The individual traces correspond to the last scan under RF modulation. We

normalize these traces to the maximum amplitude of the modes before *any* modulation is applied (*i.e.*, before taking data in Fig. S7e). Operating our EOM at the DC π phase point, we approximate peaks in the spectra as mode locations. We track the center mode's location and observe drift on the order of half of a linewidth under high-power modulation. After turning off RF modulation, the modes relax to their initial locations. There is an initial offset drift in the mode location at each RF power, which we believe occurs on a timescale shorter than the speed at which we extract data from the VNA.

This measurement scheme is useful for in situ mode characterization, as the mode behavior can be observed nearly independently of such effects as the optical power or the laser sweep rate (which changes intra-cavity optical power). The VNA/EOM sweeps are rapid and low-power, yielding an almost constant optical energy into the modes, and visualizing what appears to be steady-state mode behavior. This steady-state changes for different laser pump amplitudes, DC bias voltage, or RF power, but is independent of the VNA sweep rate or power applied to the EOM. We believe mode drift and distortion are functions of pump depletion and on-chip heating at high RF modulation powers.

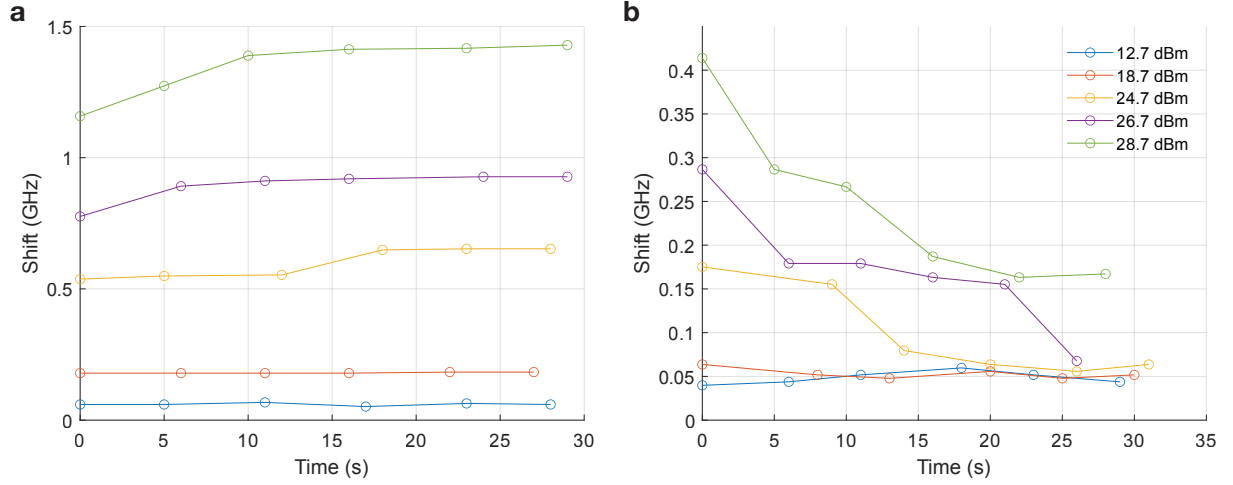


FIG. S6. **Mode drift as a function of time.** (a) Drift under RF modulation. (b) Relaxation when RF modulation is turned off. In both cases, the shift corresponds to drift of the central mode peak relative to its initial frequency prior to any modulation.

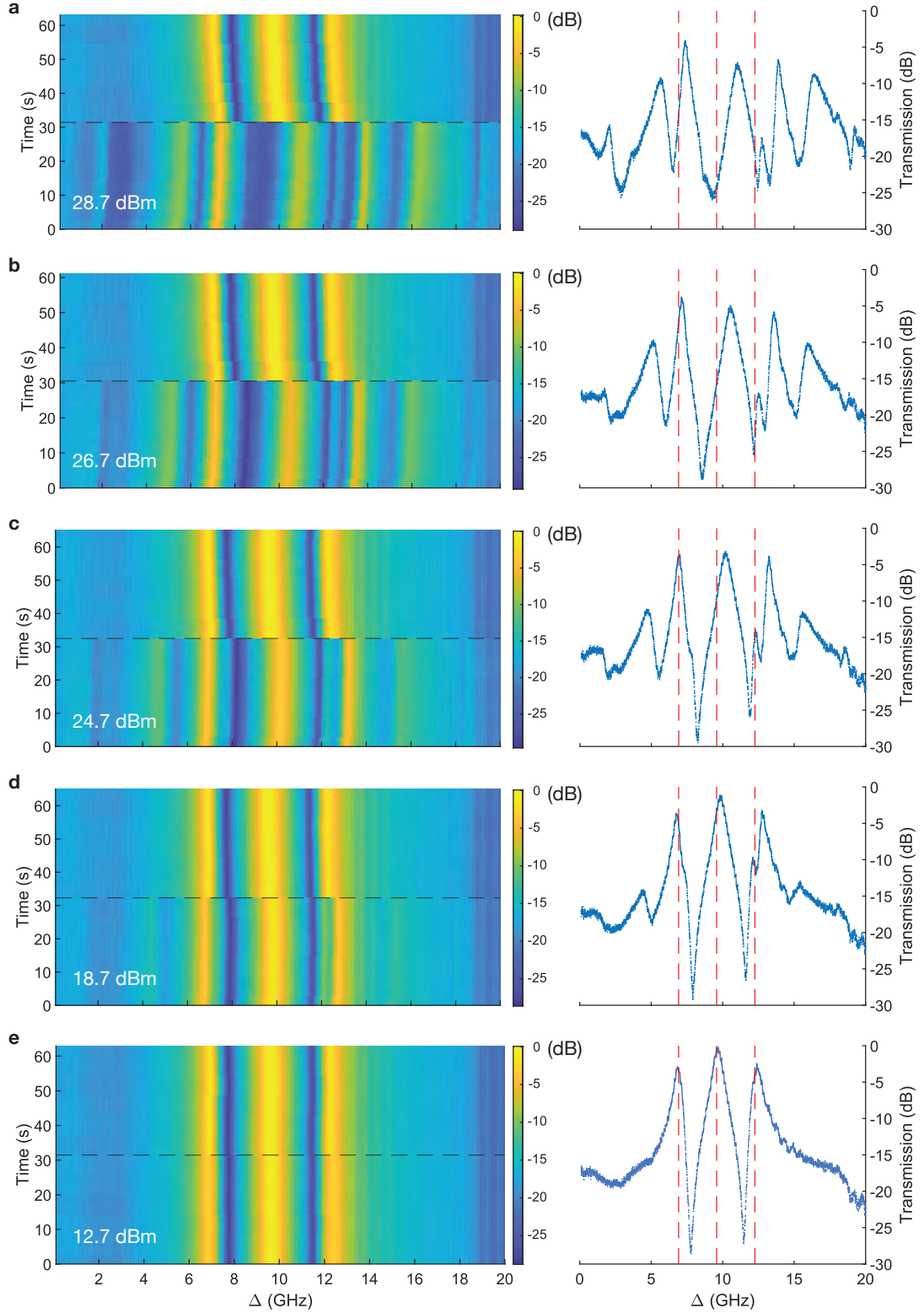


FIG. S7. **Mode drift and pump depletion under RF modulation.** Repeated VNA spectra taken over time for the RF drive powers indicated on each heatmap. The dashed black lines in each heatmap indicate the time at which modulation is turned off. Plots to the right correspond to the VNA trace taken just before modulation is turned off (i.e., the horizontal slice of the heatmap at the dashed black line). Red dashed lines in the traces correspond to the initial peak locations prior to turning on any RF modulation.

S4 DETUNING EFFECTS

A. Microwave Detuning

It is inefficient to drive the inter-band transitions with an RF tone that is detuned from the inter-band coupling rate ($\Omega = \mu + \delta$). Doing so shifts the phase condition required to achieve maximum isolation, and the converted sideband shape becomes asymmetric. This effect is exacerbated when there is disorder in the mode hybridization. In this case, one inter-band transition better matches the RF drive frequency than the other, leading to more efficient conversion at this transition. The amplitudes of the converted sidebands differ, altering the power-matching condition required for isolation.

We detune the microwave drive from the ideal value and observe changes in lineshape and fluctuations in the isolation parameter, as depicted in Fig. S8. These plots are measured for microwave drive amplitudes and frequencies as given in table S1 B.

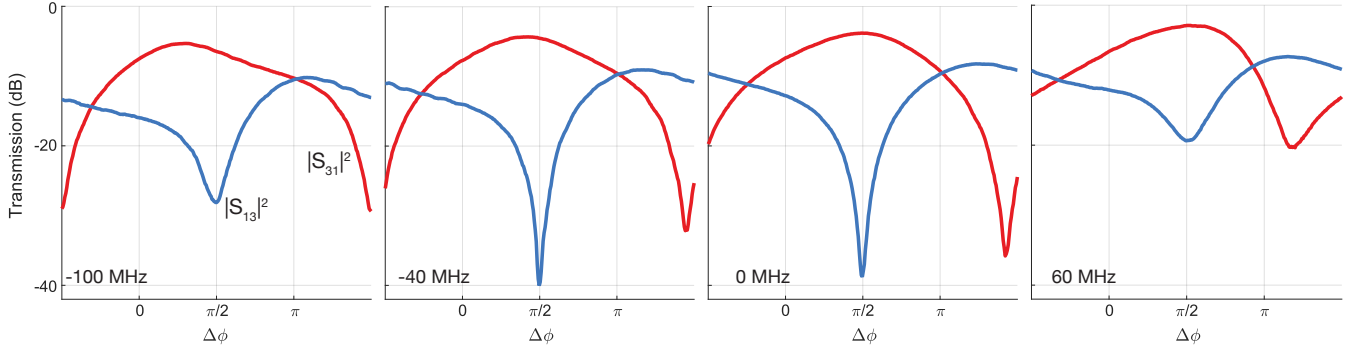


FIG. S8. **Microwave Detuning Effects.** $|S_{31}|^2$ (red) and $|S_{13}|^2$ (blue) as a function of the phase condition, $\Delta\phi = 2\phi_1 - \phi_2$, for varied RF modulation detuning, as indicated on each panel.

B. Laser Detuning and Isolation Bandwidth

Detuning the optical signal from the resonance location has a similar effect as RF detuning on the S_{ij} lineshapes and isolation parameters. There is disorder in the hybridization, evidenced by misalignment between the maximum isolation and the resonance condition. From coupled mode theory, we can predict the isolation bandwidth at the ideal power matching condition A_1 and A_2 , as given in the main text. For input and output frequencies detuned from the signal frequencies by $\Delta = \omega - \omega_i$, isolation parameters in the ideal system (*i.e.*, no disorder in the mode hybridization) are given by:

$$\begin{aligned} I_{31} &= 1 + \left(\frac{\kappa_1 + \kappa_3}{2\Delta} \right)^2 = 1 + \left(\frac{\gamma_2}{\Delta} \right)^2 \\ I_{23,12} &= 1 + \left(\frac{\kappa_1 + 2\kappa_2 + \kappa_3}{4\Delta} \right)^2 = 1 + \left(\frac{\gamma_{1,3}}{\Delta} \right)^2 \end{aligned} \quad (14)$$

The 3 dB isolation bandwidth (FWHM) is given by twice the linewidth of the intermediary mode in the indirect transition pathway. In practice, our modes have disorder and exhibit some drift with RF drive power. We observed isolation that remained within a few dB of maximum over hundreds of MHz.

S4. OPTICAL POWER IN THE CAVITY

We characterize optical power in the three resonators. Following the procedure set out by,³⁵ we drive the EOM at various bias points, pass the output through a fiber Fabry-Perot filter (Micron Optics FFP), and record the transmission on a photodiode. The transmission is depicted in Fig. S9. By comparing the sideband and carrier amplitudes after subtracting the detector noise floor, we identify how much light is scattered into sidebands for given modulation frequencies. We fit the scattering efficiency over a few drive frequencies to interpolate how much light is scattered into sidebands at the frequencies used in this experiment. By measuring the input power to the device (2.246 mW) and assuming equivalent coupling efficiency on the input and output of the device (8.14%), we determine that approximately 5.1 uW (4.3 uW and 3.6 uW) of light propagates in the feed waveguide for signals at ω_1 (ω_2 and ω_3). We use the input-output formalism presented in section S1 A to determine the flux into the first racetrack coupled to the waveguide:

$$|\hat{a}_1|^2 = \frac{\kappa_e}{\left| D_1 + \frac{\mu_{12}^2}{D_2 + \frac{\mu_{23}^2}{D_3}} \right|^2} |\alpha_{in}|^2 \quad (15)$$

$$E_{res} = \hbar\omega |\hat{a}_1|^2 \quad (16)$$

$$D_i = i\Delta' + \frac{\kappa_i}{2} \quad (17)$$

Substituting for the input flux, $|\alpha_{in}|^2$, in terms of optical power, we can solve for the circulating power in the first resonator:

$$P_1 = E_{res} \frac{v_g}{l} = \frac{\kappa_e v_g}{l \left| D_1 + \frac{\mu_{12}^2}{D_2 + \frac{\mu_{23}^2}{D_3}} \right|^2} P_{wg} \quad (18)$$

In this expression $\kappa_1 = \kappa_e + \kappa_{1,i}$ and P_{wg} refers to input signal power at a signal frequency ω_i propagating in the waveguide. We can similarly solve the input-output relations to obtain expressions for the power circulating in the second and third resonators:

$$P_2 = \left| \frac{-i\mu_{12}}{D_2 + \frac{\mu_{23}^2}{D_3}} \right|^2 P_1 \quad (19)$$

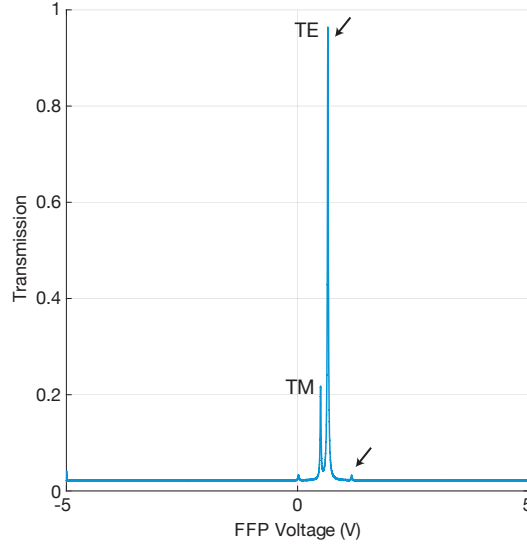


FIG. S9. **Normalized EOM response filtered by Micron Optics Fiber Fabry-Perot (FFP).** By sweeping the voltage applied to the filter, the FFP cavity frequency is swept across the EOM carrier tone and sidebands. The central response exhibits two supported polarizations in the filter cavity, and the EOM carrier tone and first sidebands are visible (indicated by arrows). Here, modulation applied to the EOM is 1 GHz.

TABLE S2. Average circulating power in resonators

Signal Frequency	Input Power (μ W)	Res. 1 (mW)	Res. 2 (mW)	Res. 3 (mW)
ω_1	5.07	77	187	111
ω_2	4.33	127	1.92	127
ω_3	3.59	72	123	52

$$P_3 = \left| \frac{-i\mu_{23}}{D_3} \right|^2 P_2 \quad (20)$$

From equations 18,19,20, using the average fit parameters obtained in section S1, we obtain power in resonators 1,2, and 3 for various signal frequencies (table S2).